Hindawi
Journal of Sensors
Volume 2020, Article ID 5609168, 14 pages
https://doi.org/10.1155/2020/5609168

Research Article

Geometrical Properties of Spilled Oil on Seawater Detected Using a LiDAR Sensor

JungHwan Moon and Minwoo Jung

CARNAVICOM Co., Ltd., R&D Center, 21984, Republic of Korea

Correspondence should be addressed to Minwoo Jung; jungminwoo80@gmail.com

Received 10 October 2019; Revised 18 November 2019; Accepted 17 December 2019; Published 1 February 2020

Academic Editor: Xavier Vilanova

We report on a small-size light detection and ranging (LiDAR) sensor, which offers the possibility of being used in the field during oil spill incidents. In the present study, we develop an algorithm that can distinguish between seawater and oil through the use of a laser at 905 nm wavelength. We investigate the ability of the sensor to detect three different oil types (light crude, bunker A, and bunker C) through experiments and analyze the differences between the types and volumes of spilled oil (1, 5, 10, 15, 20, 25, 30, 35, 40, and 50 mL). The results showed that our algorithm for detecting oil spills over seawater was successful: the LiDAR sensor was able to detect different oil types and volumes. Spilled oil area coverage ranged by more than 50% of the detected area, and the viscosity of bunker C oil reached up to 73%. In addition, the experimental oil spills were mainly formed of oil films of 1 mm and 2 mm thicknesses, which confirmed geometrical properties. Follow-up research should further investigate the characteristics of oil slick thickness measured by the LiDAR system and undertake field tests to assess the feasibility of using the LiDAR system in pollution incidents.

1. Introduction

Economic development generally results in an increase in volume of marine transportation, which subsequently increases environmental pollution of the ocean [1]. In particular, oil spills from vessels can cause disastrous pollution and can result from incidents that are a consequence of various factors including weather conditions and human error. Such incidents can in turn lead to social and economic damage as well as environmental pollution. In the case of oil spills, it is therefore very important to respond quickly to the vessels involved. Historical incidences of oil spills have highlighted the need for a method that can quickly recognize information on the spilled oil in order to facilitate prompt, active response activities. In 2017, there were 250 small incidents in Korea (<1 kL), which accounted for 92.3% of the total incidents [2].

At the outset of an incident, reports relating to various conditions are vital to establish the nature and scale of pollution. Gaining an understanding of the spilled oil amount is an important element of an effective response to most oil spills, both for assessing the location and extent of oil contamination and for verifying predictions of the movement and fate of oil slicks at sea [3].

At present, oil spills are observed using satellites and aircrafts, and their diffusion paths are subsequently predicted using computer simulations. However, satellites are expensive to use and only provide very limited information. Furthermore, computer modeling of the spread of the oil spill is associated with uncertainties since the results are based on the input conditions for the environmental and oil spill parameters.

A variety of techniques have been investigated for detecting marine oil spills, including a mass analysis method of oil types and components [4], ultraviolet (UV) fluorescence measurement with detection of electrical properties of water and oil [5, 6], measurement of volume changes in silicone rubber against oil [7], and detection using differences in absorbance [8–11].

Cameras relying on visible light are widely used to record the distribution of oil on the sea surface; however, they are affected by it being either day or night. The most commonly employed combinations of sensors include side-looking

airborne radar (SLAR) and downward-looking thermal infrared (IR) and ultraviolet (UV) imaging systems. Other systems such as forward-looking infrared (FLIR), microwave radiometers (MWR), laser fluorosensors (LF), and compact airborne spectrographic imagers (CASI) may also provide information [3].

UV, thermal IR, FLIR, MWR, and CASI are passive sensors that measure emitted or reflected radiation. With the possible exception of MWR, they are unable to penetrate cloud cover, fog, haze, or rain. MWR can provide information on the thickness of oil on the sea surface but are unable to do so if oil has emulsified. Radar systems can penetrate cloud and fog, during the day or night, and can operate under most conditions, although they are less effective both in calm conditions and in strong winds. However, radar imagery often includes a number of anomalous features or false positives, which can be mistaken for oil, such as sea ice, algae blooms, wind shadows, and rain squalls, and thus requires expert interpretation [3].

Furthermore, while advances in technology have reduced the size of equipment, many remote sensing systems are bulky and can only be used from dedicated aircraft in which they are installed. Many of these methods also require the development of additional functions such as an activation source and image processing for detection. In addition, existing methods often require extra equipment, for example, a frequency generator, a spectrum analyzer, and a capacitance meter. Although it is possible to detect water and spilled oil using the aforementioned methods, technical limitations (i.e., equipment size, data processing functions, and extra equipment) occur when they are applied in situ to real spill incidents.

The LiDAR involves the use of a laser that is mounted on an aircraft, drone, ship, or other fixed platform in various water environments including the ocean, coasts, rivers, and estuaries. LiDAR can be applied to various situations, for example, for obstacle detection for specific parameters [12, 13], estimation of floater concentrations on the surface ocean [14], verification of satellite measurement data [15–17], observations of vessel circumference/object detection, and the development of algorithms for recognizing and tracking the position of ships [18–20].

The LiDAR is able to operate normally in cloud cover, fog, haze, or rain, during the day and night [21–26], and has been miniaturized sufficiently to allow it to be installed in a small-size drone or boat [27, 28]. The detected data is also intuitive upon viewing such that that expert interpretation is not required [29–36]. The LiDAR sensors have a much higher measurement distance and special resolution in comparison to microwave equipment. In addition, it offers the advantage of being able to measure 2D and 3D spatial distributions in real-time detection.

In this study, we aimed to address the limitations of weather conditions, expert interpretation, device size, and cost by using a small-size LiDAR, which can potentially be used quickly in the field during oil spill incidents and offers the possibility of being installed in various types of equipment. We outline an algorithm that we developed to distinguish between seawater and oil through the use of a laser at 905 nm wavelength. We further investigate the differences between the types and volumes of spilled oil through experiments and analysis of the results.

2. Materials and Methods

2.1. Measurement Method. In the present study, the LiDAR system (a three-channel scanning method) using a near-infrared 905 nm wavelength laser was designed to sense oil on the surface of seawater.

The LiDAR sensor was originally developed in the 1960s following the invention of laser and distance measurement technology. Since the 1970s, the LiDAR sensor has been developed and applied to various fields, and its scope has been expanded to applications such as aerial mapping, ship design and manufacturing, and meteorological observation, as well as having been installed in spacecraft and exploration robots.

LiDAR is a remote detection and ranging method that works much like radar, emitting infrared light pulses instead of radio waves and measuring how long they take to come back after hitting nearby objects. The time between the output laser pulse and the reflected pulse allows the LiDAR sensor to calculate the distance to each object precisely, based on the speed of light. LiDAR captures millions of such precise distance measurement points each second, from which a 3D matrix of its environment can be produced. Information on objects' position, shape, and behavior can be obtained from this comprehensive mapping of the environment [37] (Figure 1).

The efficiency of the radiating and receiving beams depends on the optical path. The LiDAR uses a laser diode to shoot from a point light source, and beam collimation is enhanced with a reflective optical system, as opposed to a refractive optical system. Figure 2 shows the design of the optical path based on a reflecting optical system. In the design, the laser beam is radiated horizontally by a scanning method. Each triangular mirror is designed with angles of -1°, 0°, and 1°. By implementing different mirror angles, three channels can use a single laser diode.

The LiDAR used in this paper senses the range of 120° horizontal FOV and 2° vertical FOV in 3 channels by 30 Hz scanning frequency (Table 1).

When sensing a surrounding area, the LiDAR receives data returned from the target among each point of the shot laser. The received laser points are displayed in real time according to the reflected time and position, and each point can subsequently be displayed in either 2D or 3D, as illustrated in Figure 3.

In this study, a laser beam is reflected or refracted when they come into contact with the surface of seawater and oil; some of them return to the LiDAR and allow the distance to be measured. To measure the thickness of an oil slick, the sensing conditions of the seawater surface were first analyzed. The distance between the LiDAR and the seawater surface was then calculated as the difference in the oil thickness (Figure 4). The LiDAR continuously senses the seawater surface. When an oil slick is detected, the difference in distance that the LiDAR measures between the surface of the slick and

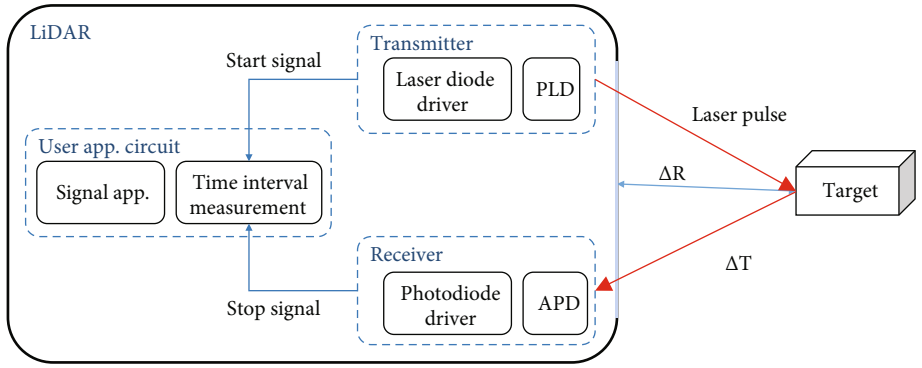

Figure 1: Principle of LiDAR.

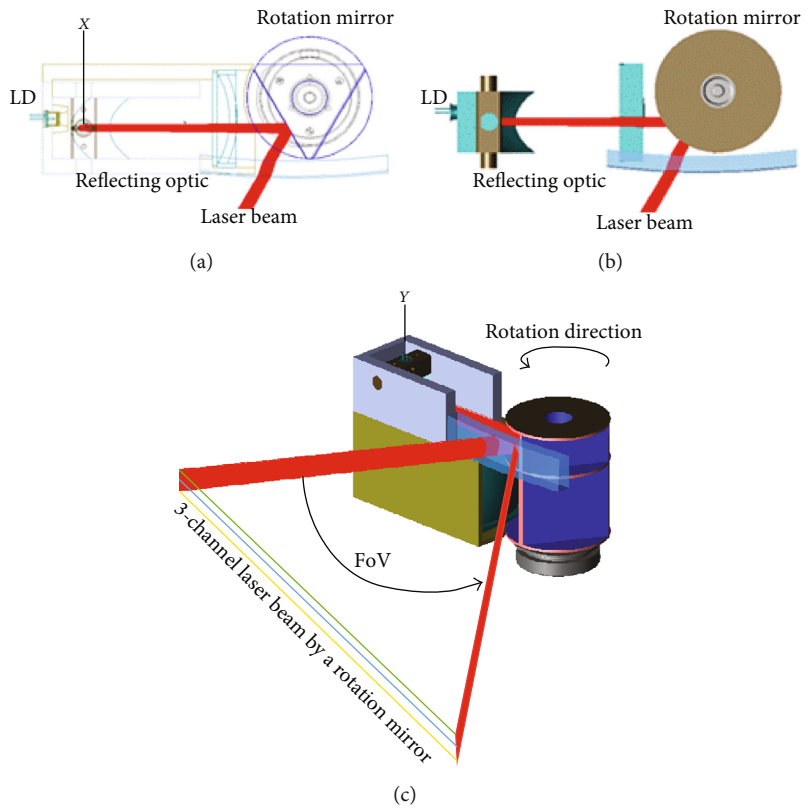

Figure 2: Optical path based on a reflecting optic of LiDAR: (a) drawing data; (b) rendering data; (c) three-channel laser beam by a rotation mirror.

Table 1: The three-channel LiDAR specification.

Items	Description	Product
Channels	3 channels	
Light source	905 nm	
Horizontal FOV and resolution	120°/0.125°	
Vertical FOV and resolution	2°/1°	
Scanning frequency	30 Hz (max.)	
Input voltage	DC 10~32 V	
Detection range	Up to 100 m	
Dimension (mm)	127 (W) × 66 (D) × 70 (H)	

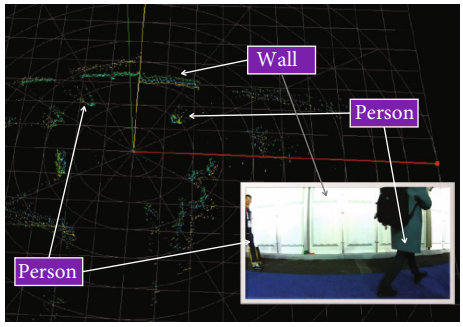

Figure 3: Sensing a surrounding area with LiDAR.

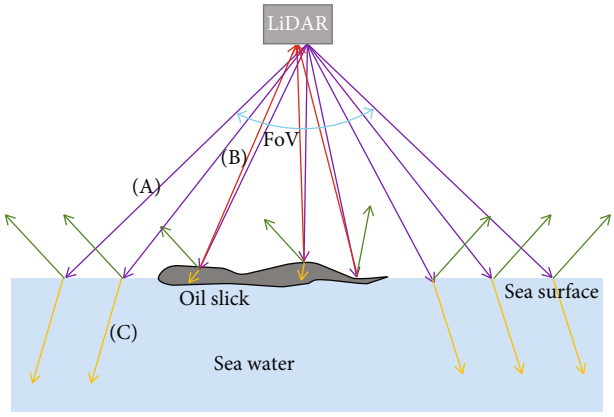

Figure 4: Oil thickness is determined from laser beams reflected by an oil slick; red lines indicate reflected beams, and yellow lines indicate absorbed beams.

the surface of the surrounding seawater is used to determine the slick thickness. Because LiDAR data may be reflected on the seawater surface, the spilled oil is identified by the detection algorithm.

The LiDAR system was used to sense seawater only (Figure 5(a)) and then seawater plus one of the three types of oil that are the major oils involved in oil spills caused by ships: light crude oil, bunker C oil, and bunker A oil (Figure 5(b)). Three separate experiments were carried out using 20 mL of each oil to investigate oil thickness. Then, experiments were carried out for each oil at increasing volumes (1, 5, 10, 15, 20, 25, 30, 35, 40, and 50 mL) in order to investigate oil diffusion. The experiment was conducted in an environment where normal exposure to sunlight and exposure to an electric lamp were set up to mimic natural conditions.

A test jig was made to carry out and record the LiDAR measurements (Figure 6). The LiDAR system was fixed to the upper part of a sensing case, and the water tank was placed in the bottom. The LiDAR system was maintained at a distance of 1.03 m above the water tank surface. The test sensing time was 10 seconds, and sensing measurements were taken 8 times per second, thereby allowing for a total of 180000 measurements (i.e., 750 points/1 channel × 3 channels × 8 times/s × 10 s).

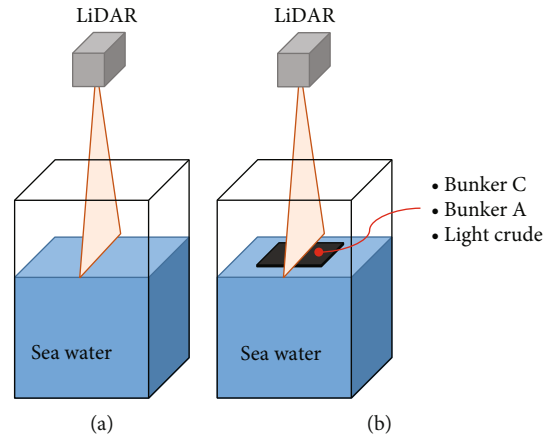

Figure 5: Illustration of the LiDAR (light detection and ranging) sensor experimental set-up for (a) seawater only and (b) the set-up using different oils (bunker C oil, bunker A oil, or light crude oil) on seawater.

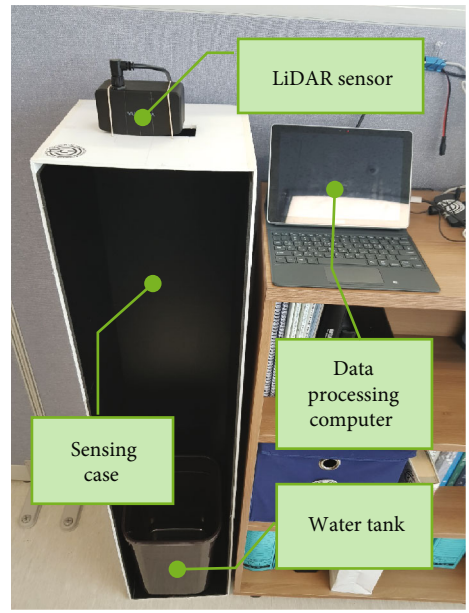

Figure 6: Test jig set-up used in this study.

2.2. Spilled Oil Detection Algorithm. In order to determine the correct continuity of oil spilled on the seawater surface in the experimental set-up, a laser point was projected in a two-dimensional space in the viewer program. We judged the projection of the laser beam based on information such as distance and angle from the position matrix. This method would not be suitable for real-time classification because it would require large computational and resource requirements; hence, we classified the distances between the points measured by the LiDAR laser using trigonometry. We then computed the distances between the LiDAR device and the points to establish an algorithm for determining the continuity of oil spillage. The LiDAR system used in the present study had a horizontal field of view (FoV) of 120° and was

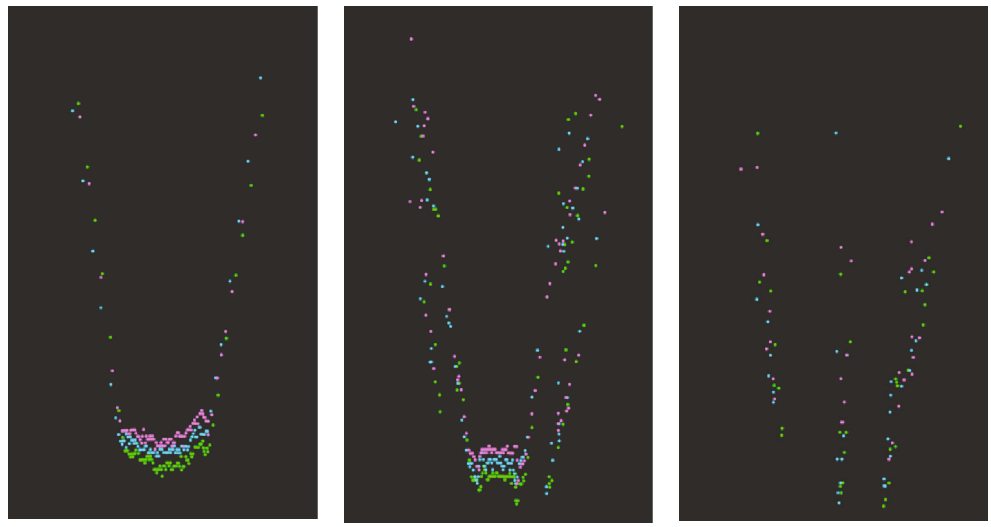

(a) (b) (c)

Figure 7: Default settings for the sensing test: (a) LiDAR data measured the sensing case inside, (b) LiDAR data with a measured empty water tank the sensing case inside, and (c) LiDAR data with measured seawater in a water tank the sensing case inside.

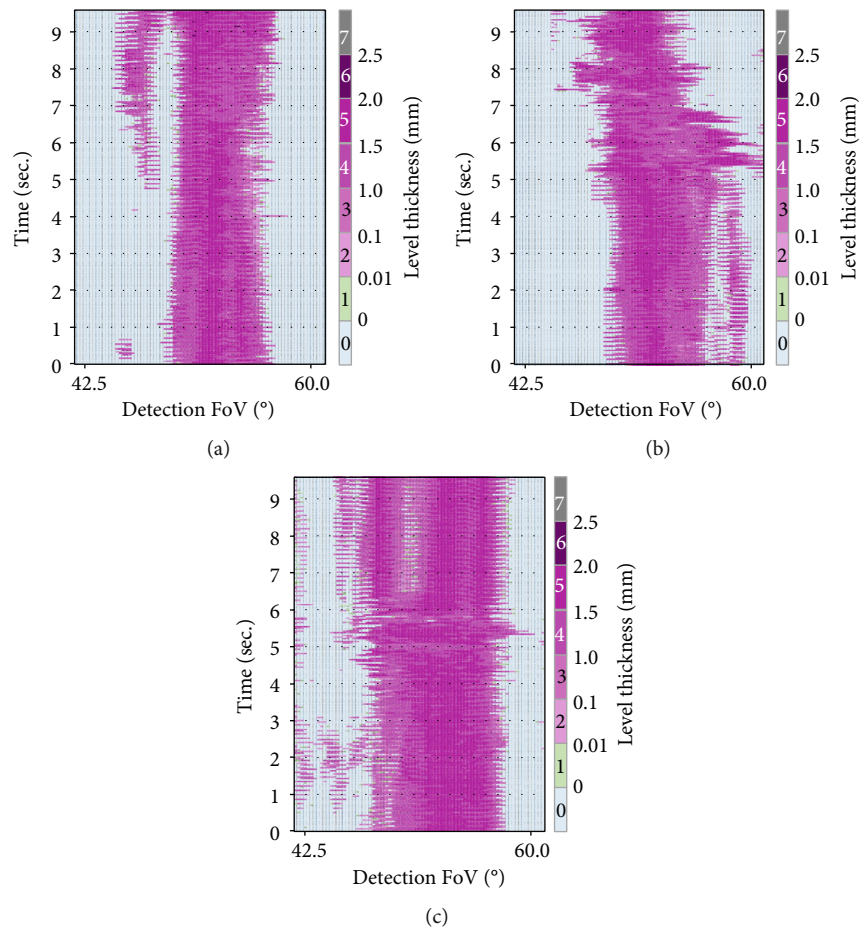

Figure 8: 20 mL spilled oil measurement experiment over time: (a) light crude, (b) bunker A oil, and (c) bunker C oil.

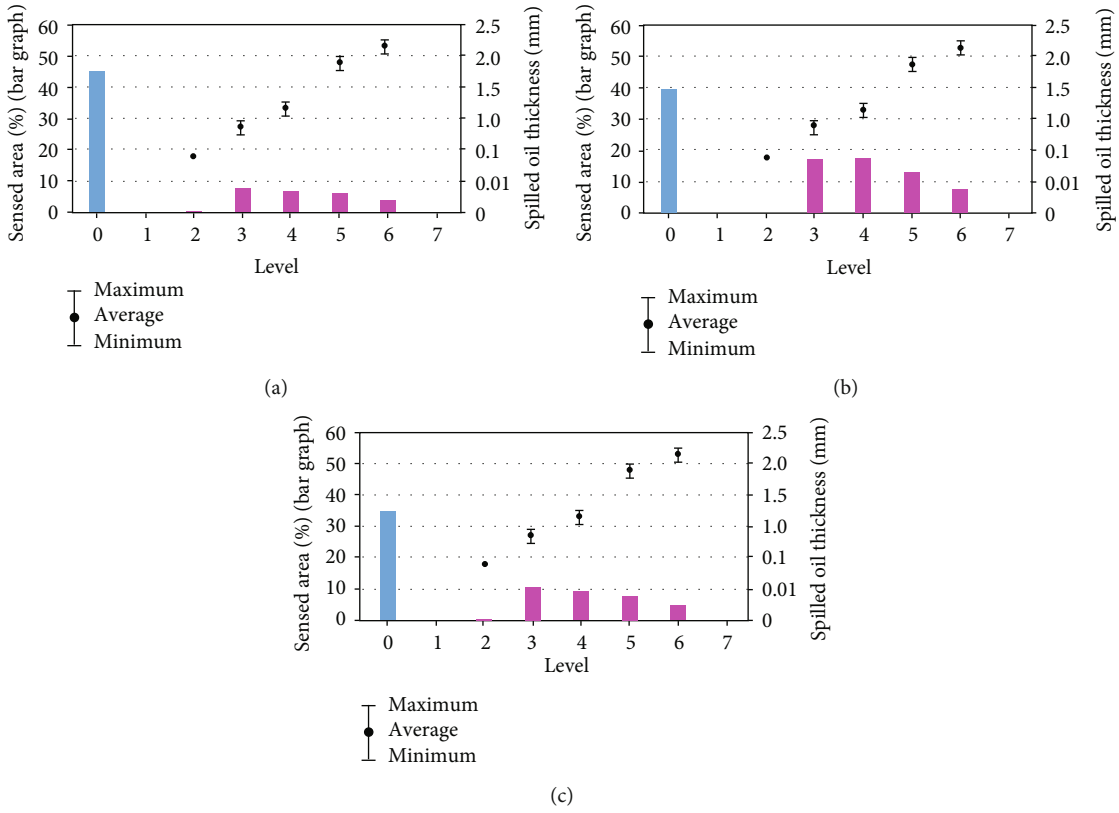

FIGURE 9: Spilled oil distribution by level and thickness: (a) light crude oil, (b) bunker A oil, and (c) bunker C oil.

able to measure 750 points. The distances between the points and the angles between them can be calculated using

$$D_{ij} = \sqrt{\left(D_j \times \sin\left(\angle_{ij}\right)\right)^2 + \left(D_i - D_j \times \cos\left(\angle_{ij}\right)\right)^2}, \quad (1)$$

where D_i is the distance from point i, D_{ij} is the distance from point i to j, and $\angle_{ij}$ is the angle between points i and j.

If two calculated points exist within a certain distance, they are considered to have continuity and are added to the matrix of consecutive points. However, the determination of continuity is affected not only by effluent but also by clutter that is reflected from the sea surface. Thus, the continuity determination is deferred even if the distance between two points is not satisfied. In this case, continuity is determined by comparing the distance between the previous point and the next postponed point of the deferred point. However, if there is a situation in which it is necessary to defer it again, the distance between each point and the LiDAR system are compared as a means of determining whether the points exist at similar distances.

To minimize noise and verify continuity in a continuous point matrix of the LiDAR data, a linear regression model was used. We used Python's Pygame library to examine the implementation of the model. The minimum line and the estimated trend line that minimize the sum of the distances of the points were calculated. Each point was then projected in a two-dimensional space, and X and Y positions of each point were calculated. For this purpose, each point measures the range of 120° from the origin of the LiDAR device.

The coordinate value of point i (P_i) is defined as (P_{xi}, P_{yi}) when measuring the distance D_i from an arbitrary point P_i measured with a horizontal spatial resolution of 0.16°. The x-value decides whether the measured data at the i-th position is symmetric. In order to process the data quickly and to determine the measurement position, the values were symmetrical (+, −) based on 60°. The y-value of P_i was calculated in the same way as the x-value as shown in

$$\begin{aligned} P_{xi} &= D_i \times \cos\left(0^\circ\right) \times \sin\left(\left(\left|i - 375\right| \times 120/750\right)^\circ\right), \\ P_{yi} &= D_i \times \cos\left(0^\circ\right) \times \sin\left(\left(\left|i - 375\right| \times 120/750\right)^\circ\right), \end{aligned} \quad (2)$$

where D_i is the distance from the LiDAR to point i, and i is the number of data.

From the position matrix A obtained by calculating (P_{xi}, P_{yi}) data from the first to i-th data, a solution for minimizing $Ax - b$ can be found in order to estimate the linear regression model as shown in

$$Ax \cong b, \quad \text{where } A = \begin{bmatrix} P_{x1} & P_{y1} \\ P_{x2} & P_{x2} \\ P_{x3} & P_{x3} \\ \cdots & \cdots \end{bmatrix}. \quad (3)$$

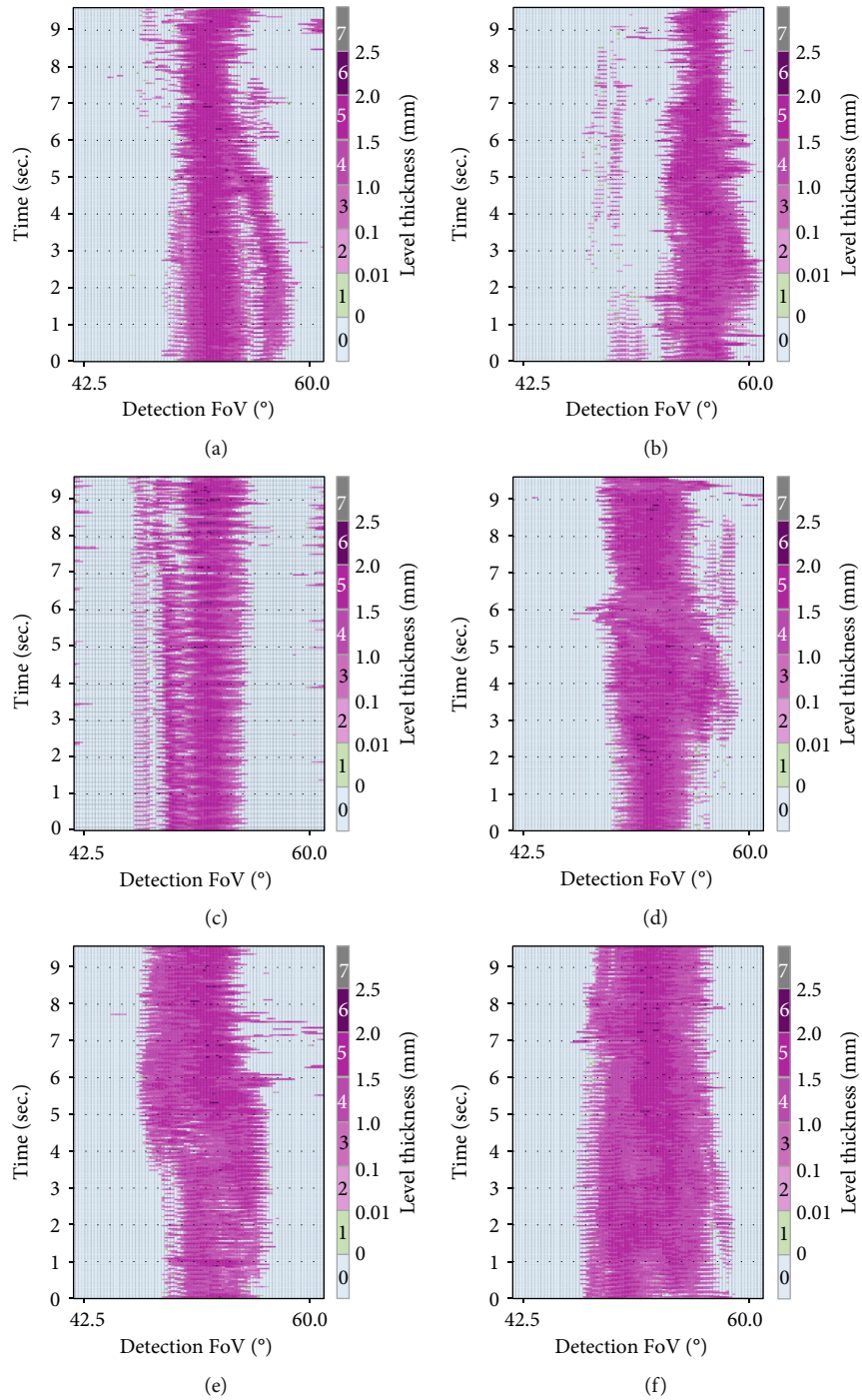

Figure 10: Spilled light crude oil measurement experiment over time: (a) 15 mL, (b) 25 mL, (c) 35 mL, (d) 40 mL, (e) 45 mL, and (f) 50 mL.

To obtain the solution of Equation (3), an upper triangular matrix is calculated as Equation (4) through an orthogonal matrix. Then, Q and R that satisfy $A = QR$ are decomposed to obtain respective values, and the results of $Ax \cong b$ are calculated as shown in Equation (5).

$$Q^T A = R, \tag{4}$$

where Q is the orthogonal matrix and R is the upper triangle matrix.

$$Q^T A = R \longrightarrow QQ^T A = QR \rightarrow \mathrm{A} = QR, \tag{5}$$

$$\therefore Ax \cong b \longrightarrow QRx \cong b \rightarrow Rx \cong Q^T b. \tag{6}$$

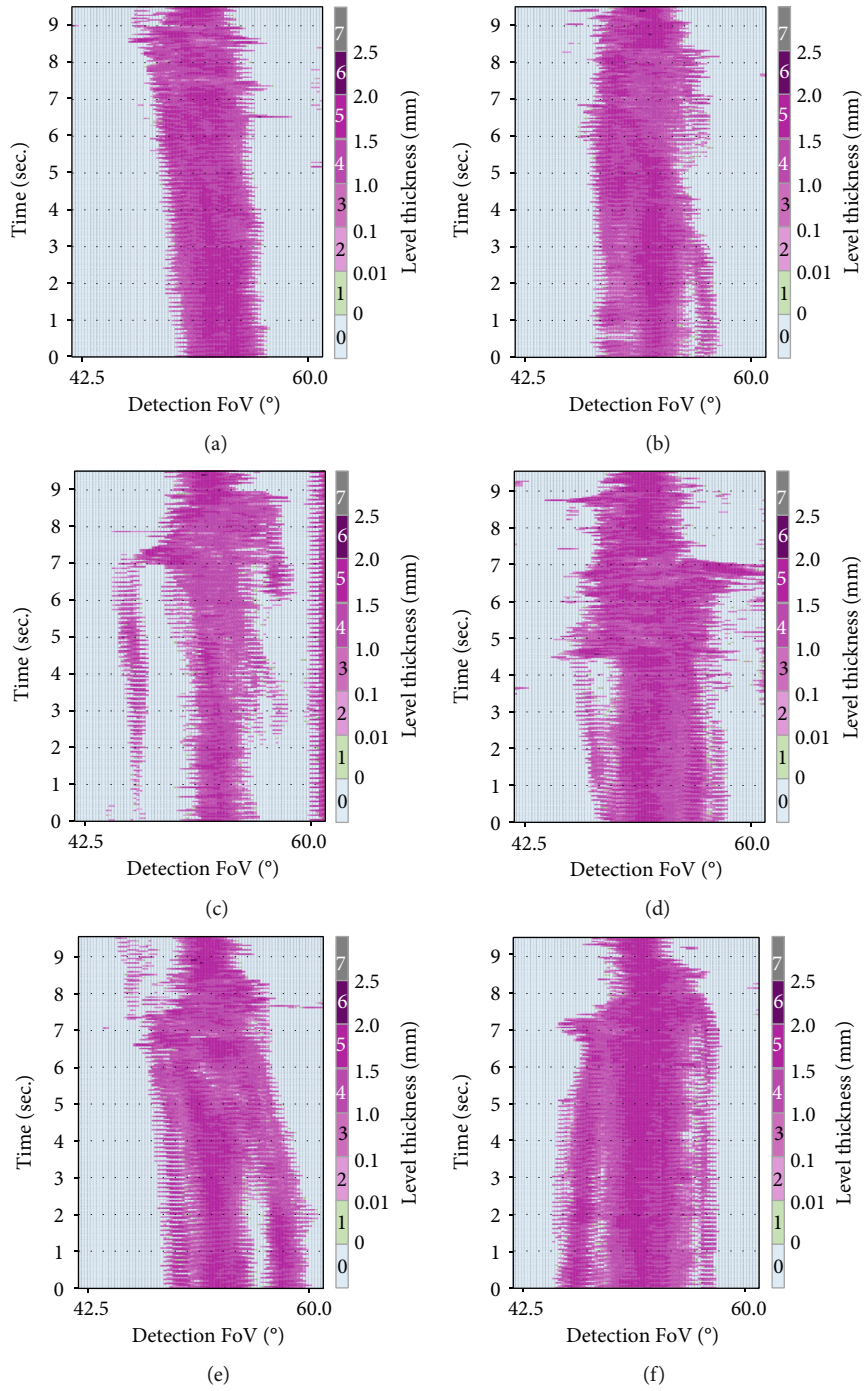

Figure 11: Spilled bunker A oil measurement experiment over time: (a) 15 mL, (b) 25 mL, (c) 35 mL, (d) 40 mL, (e) 45 mL, and (f) 50 mL.

3. Results and Discussion

3.1. Baseline Detection Experiment (Seawater Only). The baseline experiment involved using the LiDAR to measure only seawater in the water tank. The characteristics of the LiDAR mean that it is limited for sensing underwater; thus, the laser was only absorbed by the sensing case, seawater surface, and water tank case.

This sensing range was confirmed by the LiDAR system using an empty sensing case (i.e., no tank), and the sensing range for the tank was then confirmed by inserting an empty water tank into the sensing case. The seawater was subsequently added to the water tank. Figure 7 shows the resultant default LiDAR settings for the sensing case only, the empty water tank, and then seawater in the water tank. Of the total 180000 sensing data measurements, we removed unnecessary data such as the sensing case and set 25680 data measurements as the valid range where the surface of seawater was sensed.

3.2. Spilled Oil Detection Experiments. From the comparative experiments that used 20 mL of each of the three types of oil

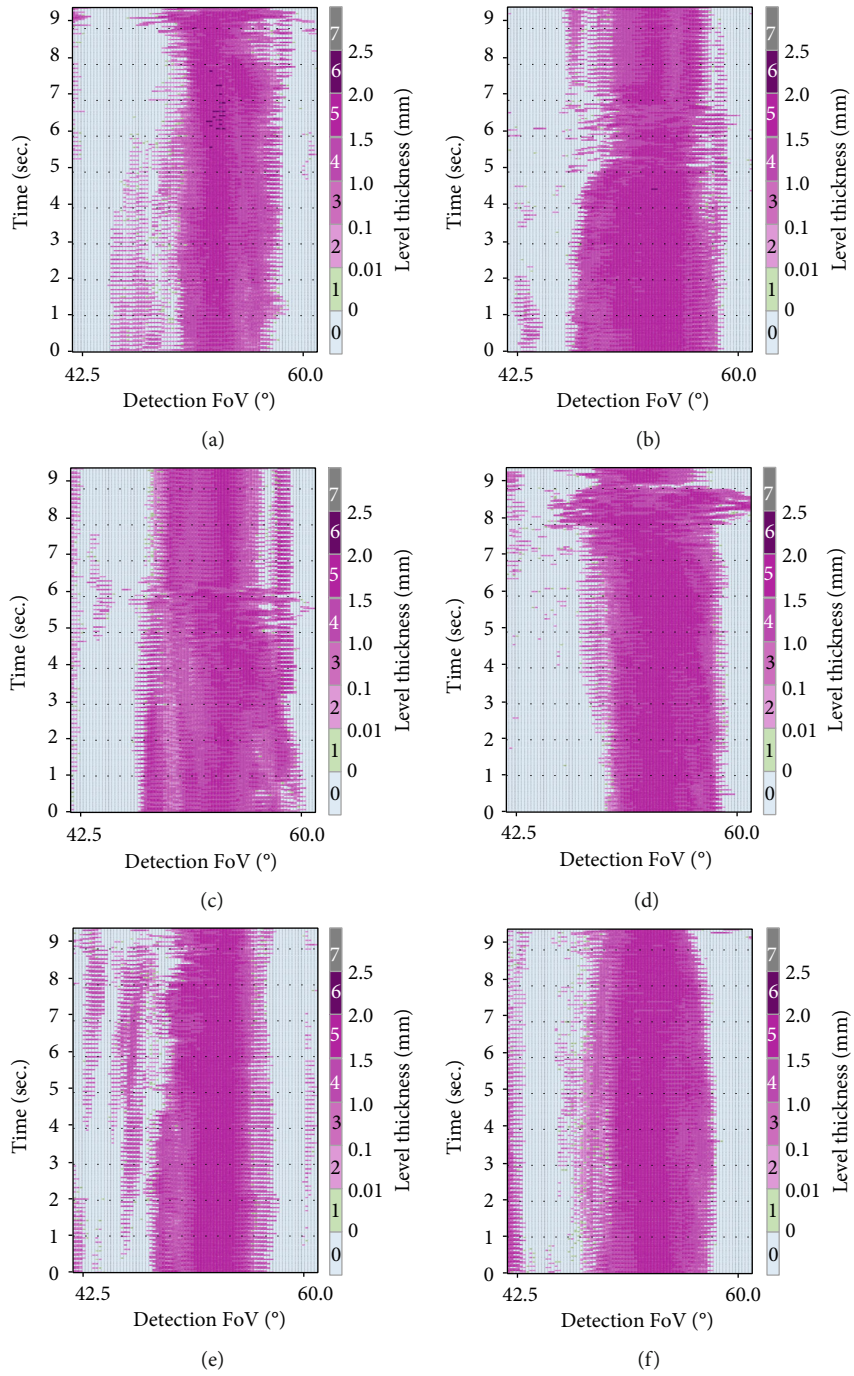

Figure 12: Spilled bunker C oil measurement experiment over time: (a) 15 mL, (b) 25 mL, (c) 35 mL, (d) 40 mL, (e) 45 mL, and (f) 50 mL.

(light crude, bunker A, and bunker C) on the seawater surface, we divided oil slick thickness into eight levels: level 0 as the surface (i.e., 0 mm), levels 1–2 as 0.01–0.1 mm, levels 3–4 as 0.1–1.5 mm, levels 4–6 as 1.5–2.5 mm, and level 7 as >2.5 mm.

Experiments demonstrated that differences in viscosity, which depend on oil type, could be sensed using the small-size LiDAR of 905 nm wavelength. The resultant measurements are shown in the viewer program as blue for water and pink for oil. Thicker oil slicks appear as darker pink in the images, whereas thinner oil appears as brighter pink, and as mentioned previously, blue corresponds to seawater (Figure 8). 20 mL of three oil types was spilled, and the occupied sensed oil area of the (i) light crude oil, (ii) bunker A oil, and (iii) bunker C was 40.49%, 58.91%, and 58.80%, respectively, for the 10-second measurement time in the total area.

The oil thicknesses were measured as levels 3–6 for all oil types. In general, the most commonly distributed oil thicknesses were levels 3–4. The area of sensed oil for the light crude oil was measured to cover >50% of the total area,

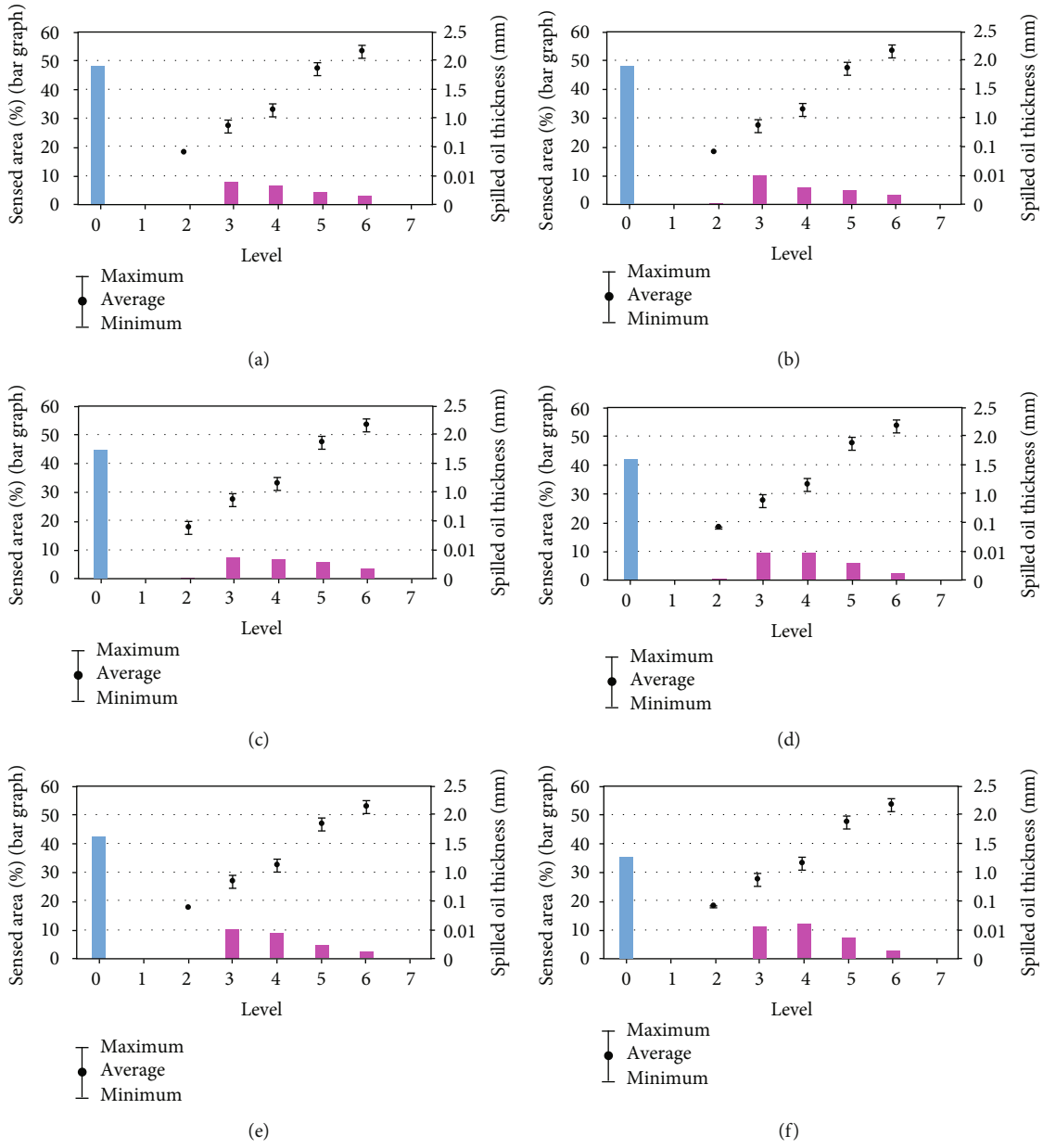

Figure 13: Spilled light crude oil distribution by level and thickness: (a) 15 mL, (b) 25 mL, (c) 35 mL, (d) 40 mL, (e) 45 mL, and (f) 50 mL.

whereas the bunker oil covered >60% of the total area. Oil thicknesses of 1 mm and 2 mm were measured most frequently (Figure 9). We determined that the 905 nm wavelength LiDAR could be used to measure the distribution and thickness of oil. The LiDAR were unable to determine thicknesses of <0.01 mm or this was can not the capabilities of the sensed.

3.3. Spilled Oil Volume Detection Experiment. The oil was detected by changing the spilled volume (15, 25, 35, 40, 45, and 50 mL) and type (light crude oil, bunker A oil, and bunker C oil), and the thicknesses were subsequently measured (Figures 10–12). We expected that as the spilled volume increased, the detection range would increase regularly. However, due to migration and diffusion of the oil slick spilled into the water tank, different characteristics were exhibited.

The sensed oil areas of coverage were measured as follows: 50–60% for light crude oil, 55–70% for bunker A oil, and 60–73% for bunker C oil in the total area. The oil slick thicknesses were distributed at levels 2–6. Even at the same capacity, the higher the viscosity, the more definitely the coverage area is considered to be high. Level 2 was mainly associated with the light crude oil, whereas the high-viscosity bunker oils (A and C) formed at level 3 and above (Figures 13–15). Therefore, through the experiments conducted in this study, the presence of oil and the thickness of oil could be measured using the LiDAR of 905 nm

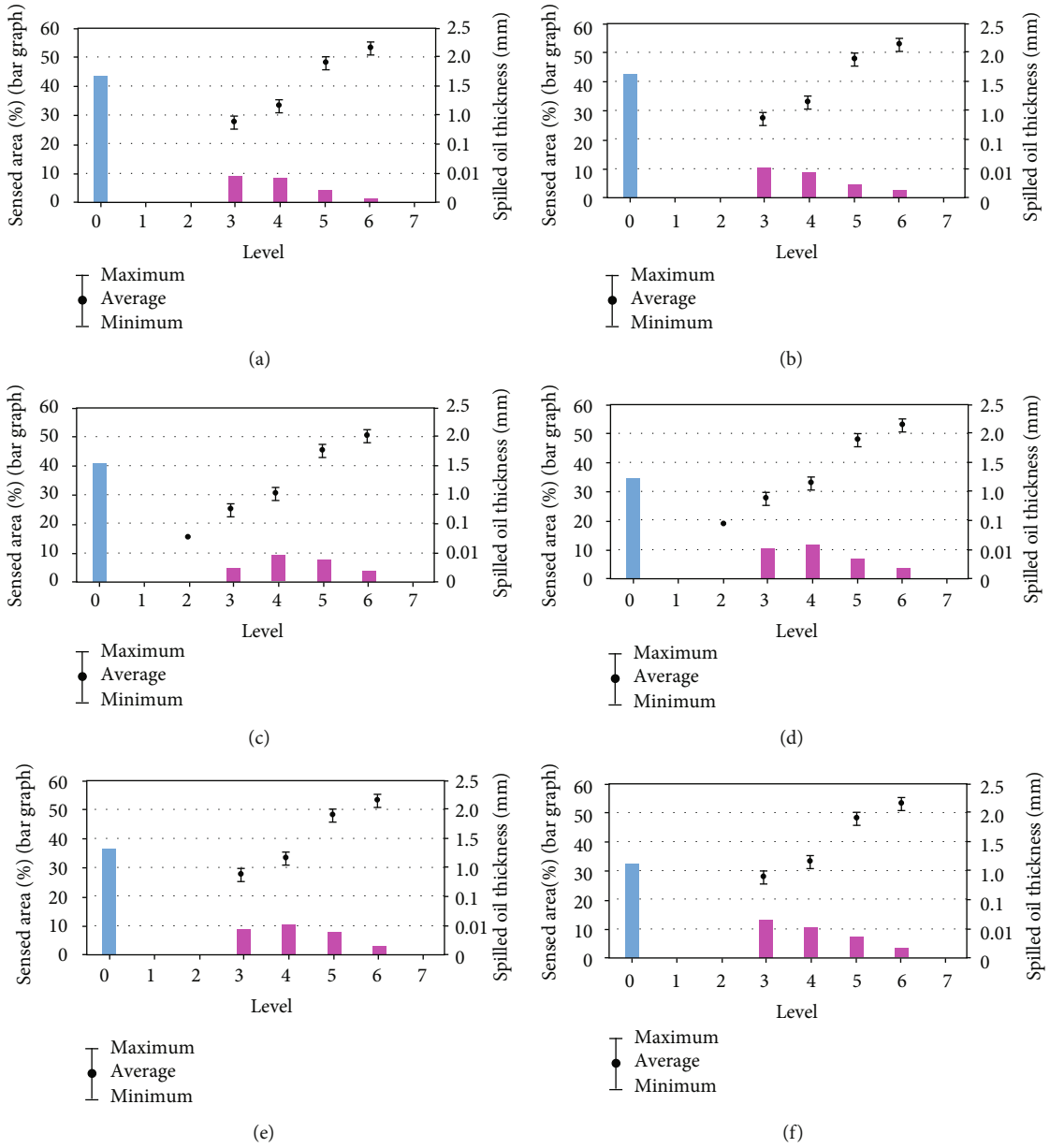

Figure 14: Spilled bunker A oil distribution by level and thickness: (a) 15 mL, (b) 25 mL, (c) 35 mL, (d) 40 mL, (e) 45 mL, and (f) 50 mL.

wavelength, and the geometrical characteristics of the oil slick could be confirmed.

4. Conclusions

In this study, we propose an algorithm for a LiDAR using a 905 nm wavelength laser for detecting spilled oil on seawater. We used an experimental set-up that mimicked natural light conditions for the sea and measured three oils that are typical for oil spill incidents. Light crude oil, bunker A oil, and bunker C oil were spilled at various volumes into seawater in a tank: 15 mL, 20 mL, 25 mL, 35 mL, 40 mL, 45 mL, and 50 mL. When sensing spilled oil, our experiments confirmed that the thickness of several stages could be measured simultaneously due to the changes in oil properties and diffusion by volume.

Depending on the oil type and viscosity, both the distributions of the detected oil slicks and the oil thicknesses were different. The LiDAR could confirm the thickness of different oils by using the algorithm presented in this study.

Spilled oil diffuses with varying thicknesses on the surface of seawater as a result of changes in oil properties and weather conditions. In our experiment, spilled oil area coverage ranged by more than 50% of the detected area, and the viscosity of bucker C oil reached up to 73%. In addition, the experimental oil spills were mainly formed of oil films of 1 mm and 2 mm thicknesses, which confirmed geometrical properties.

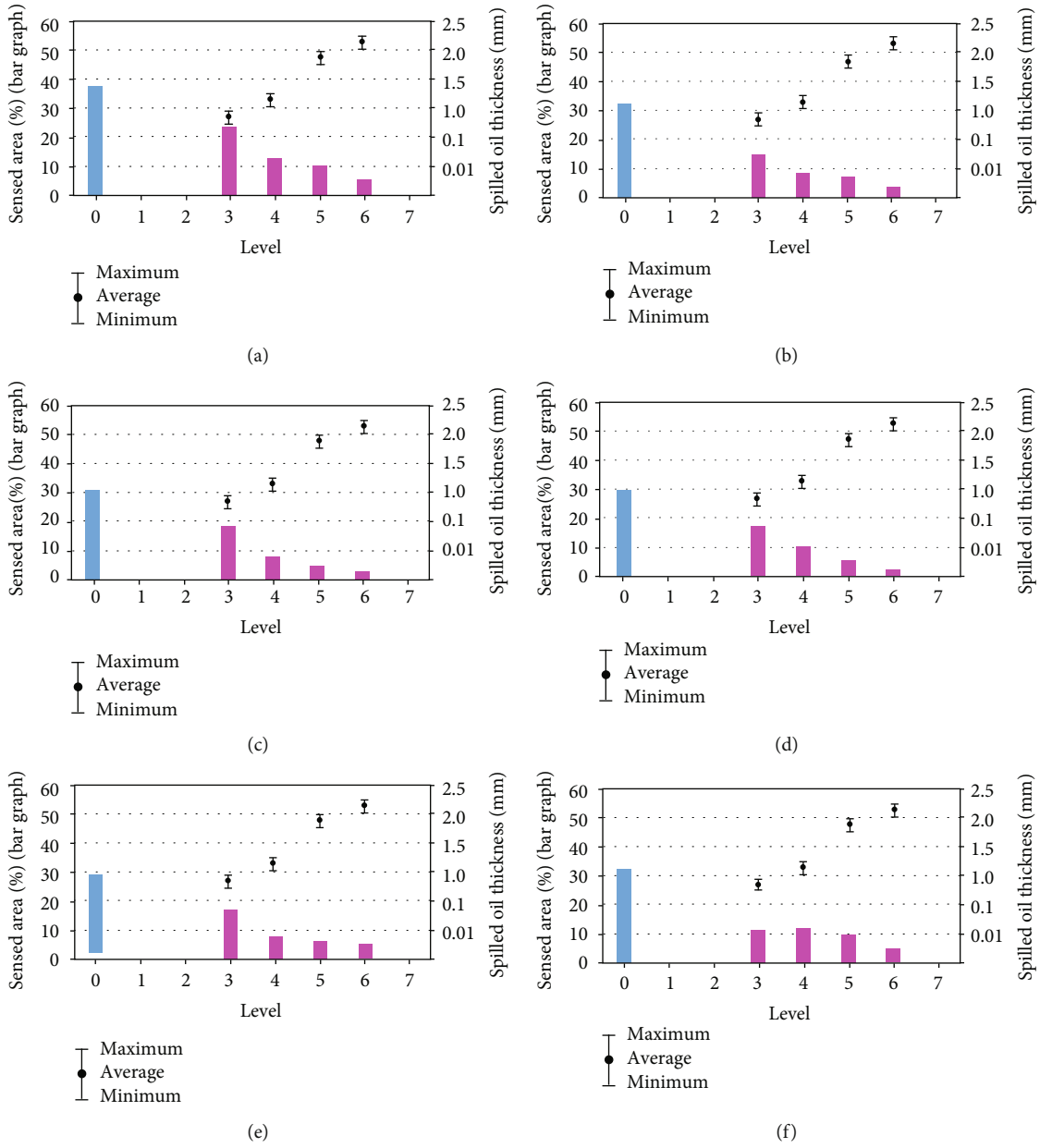

Figure 15: Spilled bunker C oil distribution by level and thickness: (a) 15 mL, (b) 25 mL, (c) 35 mL, (d) 40 mL, (e) 45 mL, and (f) 50 mL.

Hence, we conclude that our small, low-cost LiDAR using 905 nm wavelength and its algorithm offer the possibility for detecting oil spills on the surface of seawater as an alternative to larger, more expensive equipment currently used. Follow-up research should undertake a field test in order to incorporate the effects of waves and tidal currents and assess in situ feasibility for oil slicks on the seawater and should also be aimed at improving the LiDAR system performance such that it can be tested for increased detection distances and changes in oil types.

Data Availability

The sensed data used to support the findings of this study are available from the corresponding author after review of the company regulations upon request.

Conflicts of Interest

The authors declare that there is no conflict of interest regarding the publication of this paper.

Acknowledgments

This research was supported by the Basic Science Research Program through the National Research Foundation of Korea (NRF) funded by the Ministry of Education (Grant No. 2018R1D1A1B07041296).

References

[1] J. H. Moon, *The Study on Oil Spill Risk Mapping-based Marine Response Decision Support and Equipment Deployment, [Ph.D.*

thesis], Korea Maritime and Ocean University, Busan, Korea, 2018.

[2] KCG (Korea coast guard), *2018 Annual Report*, Korea Coast Guard, Korea, 2018.

[3] ITOPF, *Aerial Observation of Marine Oil Spills*, Technical Information Paper, 2017.

[4] G. Reeves, "Introduction to hydrocarbons and monitoring," in *Arjay Engineering Ltd.*, pp. 2–8, Common HydroSense Questions and General Information Guide, 2000.

[5] J. Andrews, "Automated Marine Oil Spill Detection System Development Update," *Marine Environmental Update*, vol. 97, no. 1, 1997US Navy SPARWAR Systems Centre.

[6] C. Henry and P. O. Roberts, "Background fluorescence values and matrix effects observed using smart protocols in the Atlantic Ocean and Gulf of Mexico," *International Oil Spill Conference Proceedings*, vol. 2001, pp. 1203–1207, 2001.

[7] S. Oh, M. Lee, and H. Choi, "Development of hydrocarbon oil detection sensor using the swelling property of silicone rubber," *Journal of the Korean Society for Marine Environmental Engineering*, vol. 14, no. 4, pp. 280–286, 2011.

[8] H. Denkilkian, R. Ohannessian, M. Joujou, A. Chehab, and I. Elhajj, "Wireless sensor for continuous real-time oil spill thickness and location measurement," *IEEE Transaction on Instrumentation and Measurement*, vol. 58, no. 12, pp. 4001–4011, 2009.

[9] S. W. Oh and M. J. Lee, "Oil spill detection mechanism using single-wavelength LED and CCD," *Journal of the Korean Society for Marine Environmental Engineering*, vol. 15, no. 4, pp. 323–329, 2012.

[10] S. W. Oh and M. J. Lee, "Oil thickness measurement by light absorption analysis," *Journal of the Korean Society for Marine Environmental Engineering*, vol. 16, no. 4, pp. 263–267, 2013.

[11] S. W. Oh, D. M. Seo, K. Y. Ann et al., "Oil fluorescence spectrum analysis for the design of fluorimeter," *Journal of the Korean Society for Marine Environmental Engineering*, vol. 18, no. 4, pp. 304–309, 2015.

[12] S. Babichenko, "Laser remote sensing of the European marine environment: LIF technology and applications," in *Remote Sensing of the European Seas*, V. Barale and M. Gade, Eds., pp. 189–204, Springer, Dordrecht, 2008.

[13] H. Barth, R. Reuter, and M. Schröder, "Measurement and simulation of substance specific contributions of phytoplankton, gelbstoff, and mineral particles to the underwater light field in coastal waters," *EARSeL eProceedings*, vol. 1, pp. 165–174, 2000.

[14] N. A. Aibulatov, P. O. Zavialov, and V. V. Pelevin, "Features of hydrophysical purification Russian Black Sea coastal area near the mouths of rivers," *Geo Ecology*, vol. 4, pp. 301–310, 2008.

[15] L. Fiorani, R. Barbini, F. Colao et al., "Combination of lidar, MODIS and SeaWiFS sensors for simultaneous chlorophyll monitoring," *EARSeL eProceedings*, vol. 3, pp. 8–17, 2004.

[16] L. Fiorani, R. Fantoni, L. Lazzara, I. Nardello, I. Okladnikov, and A. Palucci, "Lidar calibration of satellite sensed CDOM in the Southern Ocean," *EARSeL eProceedings*, vol. 5, pp. 89–99, 2006.

[17] F. E. Hoge, P. E. Lyon, R. N. Swift et al., "Validation of Terra-MODIS phytoplankton chlorophyll fluorescence line height. I. Initial airborne lidar results. I. Initial airborne lidar results," *Applied Optics*, vol. 42, no. 15, pp. 2767–2771, 2003.

[18] T. H. Fang, J. W. Han, N. S. Son, and S. Y. Kim, "Track initiation and target tracking filter using LiDAR for ship tracking in marine environment," *Journal of Institute of Control, Robotics and Systems*, vol. 22, no. 2, pp. 133–138, 2016.

[19] R. Halterman and M. Bruch, "Velodyne HDL-64E LIDAR for unmanned surface vehicle obstacle detection," in *Unmanned Systems Technology XII*, Orlando, FL, USA, 2010.

[20] J. H. Moon and J. J. Yun, "Development of a boat operator computer scoring system based on LiDAR and WAVE," *Journal of the Korean Society of Marine Environment and Safety*, vol. 25, no. 4, pp. 504–510, 2019.

[21] C. Dannheim, C. Icking, M. Mäder, and P. Sallis, "Weather detection in vehicles by means of camera and LIDAR systems," in *2014 Sixth International Conference on Computational Intelligence, Communication Systems and Networks*, Tetova, Macedonia, 2014.

[22] C. M. Shun and P. W. Chan, "Applications of an infrared Doppler Lidar in detection of wind shear," *Journal of Atmospheric and Oceanic Technology*, vol. 25, no. 5, pp. 637–655, 2008.

[23] B. L. Lee, E. H. Sohn, M. L. Ou, and Y. J. Kim, "Infrared spectral signatures of dust by ground-based FT-IR and space-borne AIRS," *Atmosphere*, vol. 19, no. 4, pp. 319–329, 2009.

[24] M. Weissmann, R. Busen, A. Dörnbrack, S. Rahm, and O. Reitebuch, "Targeted observations with an airborne wind Lidar," *Journal of Atmospheric and Oceanic Technology*, vol. 22, no. 11, pp. 1706–1719, 2005.

[25] S. K. Shin, Y. M. Nho, K. H. Lee, D. H. Shin, and K. C. Kim, "Retrieval of single scattering albedo for Asian dust mixed with pollution using multi wavelength Raman LIDAR system," in *Korean Society for Atmospheric Environment, 2013 Conference*, p. 118, Busan, Korea, 2013.

[26] W. Tang, P. W. Chan, and G. Haller, "Lagrangian coherent structure analysis of terminal winds detected by Lidar. Part I: turbulence structures," *Journal of Applied Meteorology and Climatology*, vol. 50, 2011.

[27] D. A. Zimble, D. L. Evans, G. C. Carlson, R. C. Parker, S. C. Grado, and P. D. Gerard, "Characterizing vertical forest structure using small-footprint airborne LiDAR," *Remote Sensing of Environment*, vol. 87, no. 2–3, pp. 171–182, 2003.

[28] K. Kimoto, N. Asada, T. Mori, Y. Hara, A. Ohya, and S.'i. Yuta, "Development of small size 3D LIDAR," in *2014 IEEE International Conference on Robotics and Automation (ICRA)*, Hong Kong, China, 2014.

[29] J. Qiu, Z. Cui, Y. Zhang et al., "DeepLiDAR: deep surface normal guided depth prediction for outdoor scene from sparse LiDAR data and single color image," in *The IEEE Conference on Computer Vision and Pattern Recognition (CVPR)*, pp. 3313–3322, Long Beach, CA, USA, 2019.

[30] J. Verrelst, G. W. Geerling, K. V. Sykora, and J. G. P. W. Clevers, "Mapping of aggregated floodplain plant communities using image fusion of CASI and LiDAR data," *International Journal of Applied Earth Observation and Geoinformation*, vol. 11, no. 1, pp. 83–94, 2009.

[31] J. Zhang, W. Xiao, B. Coifman, and J. P. Mills, "Image-based vehicle tracking from roadside LiDAR data," *The International Archives of the Photogrammetry, Remote Sensing and Spatial Information Sciences*, vol. XLII-2/W13, pp. 1177–1183, 2019.

[32] K. Johansen, L. A. Arroyo, J. Armston, S. Phinn, and C. Wittea, "Mapping riparian condition indicators in a sub-tropical savanna environment from discrete return LiDAR data using object-based image analysis," *Ecological Indicators*, vol. 10, no. 4, pp. 796–807, 2010.

[33] L. Guoa, N. Chehataab, C. Malletb, and S. Boukira, "Relevance of airborne lidar and multispectral image data for urban scene classification using Random Forests," *ISPRS Journal of Photogrammetry and Remote Sensing*, vol. 66, no. 1, pp. 56–66, 2011.

[34] N. Demir and E. Baltsavias, "Automated modeling of 3D building roofs using image and LiDAR data," *ISPRS Annals of Photogrammetry, Remote Sensing and Spatial Information Sciences*, vol. I-4, pp. 35–40, 2012.

[35] N. Demir, B. Bayram, D. Z. Şeker, S. Oy, A. İnce, and S. Bozkurt, "Advanced lake shoreline extraction approach by integration of SAR image and LIDAR data," *Marine Geodesy*, vol. 42, pp. 166–185, 2018.

[36] X. Li, X. Cheng, W. Chen, G. Chen, and S. Liu, "Identification of forested landslides using LiDar data, object-based image analysis, and machine learning algorithms," *Remote Sensing*, vol. 7, no. 8, pp. 9705–9726, 2015.

[37] "Ledder tech," September 2019, https://leddartech.com/why-lidar/.